Received: 30 May 2024 | Revised: 21 October 2024 | Accepted: 25 October 2024

DOI: 10.1002/psp4.13275

ARTICLE

Exposure–response modeling of liver fat imaging endpoints in non-alcoholic fatty liver disease populations administered ervogastat alone and co-administered with clesacostat

Jim H. Hughes[1] | **Neeta B. Amin**[2] | **Jessica Wojciechowski**[1] | **Manoli Vourvahis**[3]

[1]Pfizer Research and Development, Groton, Connecticut, USA

[2]Pfizer Research and Development, Cambridge, Massachusetts, USA

[3]Pfizer Research and Development, New York, New York, USA

Correspondence
Jim H. Hughes, Pfizer Research and Development, 445 Eastern Point Road, Groton, CT 06340, USA.
Email: jim.hughes@pfizer.com

Abstract

Non-alcoholic fatty liver disease and non-alcoholic steatohepatitis describe a collection of liver conditions characterized by the accumulation of liver fat. Despite biopsy being the reference standard for determining the severity of disease, non-invasive measures such as magnetic resonance imaging proton density fat fraction (MRI-PDFF) and FibroScan® controlled attenuation parameter (CAP™) can be used to understand longitudinal changes in steatosis. The aim of this work was to describe the exposure–response relationship of ervogastat with or without clesacostat on steatosis, through population pharmacokinetic/pharmacodynamic (PK/PD) modeling of both liver fat measurements simultaneously. Population pharmacokinetic and exposure–response models using individual predictions of average concentrations were used to describe ervogastat/clesacostat PKPD. Due to both liver fat endpoints being continuous-bounded outcomes on different scales, a dynamic transform-both-sides approach was used to link a common latent factor representing liver fat to each endpoint. Simultaneous modeling of both MRI-PDFF and CAP™ was successful with both measurements being adequately described by the model. The clinical trial simulation was able to adequately predict the results of a recent Phase 2 study, where subjects given ervogastat/clesacostat 300/10 mg BID for 6 weeks had a LS means and model-predicted median (95% confidence intervals) percent change from baseline MRI-PDFF of −45.8% and −45.6% (−61.6% to −31.8%), respectively. Simultaneous modeling of both MRI-PDFF and CAP™ was successful with both measurements being adequately described. By describing the underlying changes of steatosis with a latent variable, this model may be extended to describe biopsy results from future studies.

Trial registration: ClinicalTrials.gov NCT02871037, NCT03092232, NCT03230383, NCT03248882, NCT03309202, NCT03372044, NCT03513588, NCT03534648, NCT03597217, NCT03776175, NCT03871439, NCT04044053, NCT04091061, NCT04399538.

Study Highlights

WHAT IS THE CURRENT KNOWLEDGE ON THE TOPIC?

Ervogastat and clesacostat are both under development for the treatment of NASH, inhibiting diacylglycerol acyltransferase 2 and acetyl-coenzyme A carboxylase, respectively.

WHAT QUESTION DID THIS STUDY ADDRESS?

The description of the relationship between ervogastat and clesacostat treatment on liver fat using population pharmacokinetic and exposure–response models was assessed. The correlation between liver fat endpoints MRI-PDFF and CAP™ was estimated as part of this assessment.

WHAT DOES THIS STUDY ADD TO OUR KNOWLEDGE?

Reduction in liver fat resulting from ervogastat and clesacostat as monotherapy and combination therapy were described using an exposure–response model. MRI-PDFF and CAP™ were described simultaneously accounting for shared changes in these liver fat endpoints with a single latent variable.

HOW MIGHT THIS CHANGE DRUG DISCOVERY, DEVELOPMENT, AND/OR THERAPEUTICS?

This approach may be used for other therapeutics to incorporate all information collected on liver fat and provides a base model that could be extended to describe steatohepatitis scores measured by biopsy.

INTRODUCTION

Non-alcoholic fatty liver disease (NAFLD) encompasses a range of liver conditions characterized by hepatic triglyceride accumulation.[1] The condition often remains benign, but can lead to inflammation, hepatocellular damage, and fibrosis upon progression to non-alcoholic steatohepatitis (NASH).[2] This progression is associated with a dramatic increase in liver-specific and overall mortality rates, rising from 0.77 and 15.44 deaths per 1000 person-years to 11.77 and 25.56, respectively.[3] With the concerning growth in the prevalence of NAFLD in the United States, rising from 20% to 32% over a 20-year period,[4] and the significant economic burden associated with this disease,[5] it is clear there is an urgent need for therapies for these diseases.

The accumulation of lipids in the liver, referred to as hepatic steatosis, is a key trigger in the complex pathogenesis that culminates in NASH.[6] The measurement of this steatosis can be an important part of understanding a patient's current disease state, alongside other markers of progression. Liver biopsy is the reference-standard measurement for diagnosis of NAFLD and NASH,[7] with staging determined through histological review conducted by a pathologist. As part of broader histopathological scoring systems such as NAFLD activity score-fibrosis stage (NAS-FS)[8] or steatosis-activity-fibrosis (SAF),[9] an integer score is used to describe the extent of steatosis (0 – <5%; 1 – 5–33%; 2 – 34–66%; 3 – >67%, for both systems).

The use of liver biopsy to quantify steatosis has multiple limitations, despite its historical "gold standard" status. The invasiveness of the procedure and inter-rater variability are both significant problems.[10] While the latter can be handled through reaching a consensus between multiple pathologists, the invasive nature of a biopsy prevents repeated measurements, over time, from being performed. To circumvent this limitation, there are a growing number of non-invasive procedures to quantify steatosis using ultrasound and magnetic resonance imaging (MRI) methods, with FibroScan® controlled attenuation parameter (CAP™) and MRI-derived proton density fat fraction (MRI-PDFF) being the most common.[11,12] These measurements are both more suitable to evaluate longitudinal changes in steatosis, though are not without their own limitations with MRI-PDFF requiring expensive equipment and CAP™ being highly operator-dependent (a common limitation of all ultrasound technologies) and variable.[13]

Treatment options for NASH are currently limited, with emphasis on lifestyle modifications and managing comorbidities, and only one agent garnering conditional approval (in the USA) for the management of NASH with F2-F3 fibrosis.[14] However, many promising pharmacological therapies, targeting the root cause of metabolic dysfunction, are currently under development.[15] Amongst these agents are mechanisms that decrease de novo lipogenesis thereby decreasing hepatic steatosis, a contributor to the development of NAFLD. Ervogastat and clesacostat, which target diacylglycerol acyltransferase 2 (DGAT2) and acetyl-coenzyme A carboxylase (ACC), respectively, both play a major role in decreasing hepatic steatosis. Both drugs have shown favorable reductions in liver fat as monotherapy,[16] with an aim to administer the two drugs concomitantly resulting in an improved pharmacotherapeutic profile.

The aim of this work was to describe the longitudinal exposure–response relationship of ervogastat and clesacostat on liver fat. The use of multiple measures of liver fat is expected to improve the ability of PK/PD modeling to identify an exposure–response relationship over additional measurement times, however, the correlation between different measures of liver fat are not well explained with linear correlations[17] nor do they have consistent thresholds corresponding to individual liver fat grades from biopsy.[13,18] Simultaneous modeling of MRI-PDFF and CAP™ sought to describe the common factor described by these measurements (liver fat) exploring the correlations between the two measures and developing a model that could be extended to describe liver biopsy results from future studies.[19]

MATERIALS AND METHODS

Study data

Clinical trial data used for pharmacokinetic and exposure–response modeling were pooled from a total of 14 studies, with 9, 8, and 4 studies used for the ervogastat, clesacostat and liver fat analyses, respectively.[16,20,21] Studies consisted of 11 Phase I studies (NCT02871037, NCT03092232, NCT03230383, NCT03309202, NCT03372044, NCT03513588, NCT03534648, NCT03597217, NCT03871439, NCT04044053, NCT04091061) and 3 Phase II studies (NCT03248882, NCT03776175, NCT04399538). All study protocols, their amendments, and informed consent documentation for studies included in the analyses were reviewed and approved by institutional review boards, and all studies were conducted in accordance with Good Clinical Practice, the Declaration of Helsinki, and local regulations. A full description of each study and investigators can be found in the Tables S1 and S2. A full description of bioanalytical assays and imaging methods is listed in the Supplemental Information.

Pharmacokinetic model

Population PK models for both ervogastat and clesacostat were developed using all available plasma concentrations. Base models were developed considering one- and two-compartment kinetics, in addition to first-order, zero-order, and mixed absorption models. Base models were used to conduct covariate analysis using a full model estimation approach with pre-specified covariates.[22,23] A detailed description of the methods for population PK model development is available in the Supporting Information.

Exposure–response model

Continuous-bounded outcomes

A dynamic transform-both-sides (dTBS) approach[24] was used to normalize the distribution and constrain model predictions within the boundary of each endpoint (MRI-PDFF: 0–100%; CAP™: 100–400 dB/m). The transformation allowed model parameter values to be estimated within the scale of the transform ($-\infty$ to ∞), with model predictions being converted back to the original scale of each endpoint for interpretation (Equation 1). Full description of the equations for the calculation of the log-likelihood of transformed and boundary data is detailed in the Supporting Information.[25]

$$\begin{array}{lcll} z(y) & = & \dfrac{y-a}{b-a} & z(y)\ \epsilon\ (0,1) \\ h(y) & = & h(y,\alpha) & h(y)\ \epsilon\ (-\infty,\infty) \\ & = & \log\left(\dfrac{(1-z(y))^{-\alpha}-1}{\alpha}\right) & \alpha \neq 0 \\ & = & \log(-\log(1-z(y))) & \alpha = 0 \end{array} \quad (1)$$

where y is the observed/predicted endpoint in the original scale (linear domain), a and b are the endpoint-specific lower and upper boundaries and α is the Aranda-Ordaz transform coefficient. $z(y)$ is the first step of the transformation changing the scale of the endpoint to be bound between 0 and 1 and $h(z(y))$ is the completed transformation with no finite boundaries.

Model equations

The underlying steatosis quantified by MRI-PDFF and FibroScan® CAP™ were modeled using a latent variable approach inspired by the common factor model. The common factor model assumes that different measurements share the same underlying construct and is most often seen in factor analysis and structural equation modeling.[26,27] By making this assumption, the inter-individual variability (IIV) of these endpoints is split into the shared variance (Ψ) representing the latent construct (liver fat), and the unique variance (Σ) representing the systematic and random variation of each endpoint. These two variances are assumed to be independent. These assumptions share similarities with those made by item response theory (IRT) models,[28] with a key difference being the use of continuous data. Equations 2–5 show the parameterization of the model.

$$h\left(y_{ijk}\right) = y_{0k} + s_k \Psi_{ij} + s_k \Sigma_{ijk} \tag{2}$$

$$\Psi_{ij} = E_{pbo,ij} + E_{trt,ij} + \psi_i \tag{3}$$

$$\Sigma_{ijk} = \eta_{ik} + \epsilon_{ijk} \tag{4}$$

$$\lambda_k = \frac{\frac{1}{\omega_k} \cdot \sqrt{1 + \left(\frac{1}{\omega_k}\right)^2}}{1 + \left(\frac{1}{\omega_k}\right)^2} \tag{5}$$

where $h(y_{ijk})$ is the transformed individual prediction of the ith individual at the jth sampling time for the kth endpoint, y_{0k} is the transformed baseline population prediction, Ψ is the latent variable representing the shared change from baseline with scaling parameter, s, E represents the effects of placebo, *pbo*, and treatment, *trt*, on the latent variable, Σ represents the unique changes of each endpoint, while ψ, η and ε are independent random variables describing the shared inter-individual, unique inter-individual and unique intra-individual variability, respectively, with a mean of 0 and variance of 1, ${\omega_k}^2$ and ${\sigma_k}^2$, respectively. λ is a derived parameter used for interpretation, representing the correlation of each measure with the latent variable.

Separate transforms were required for each measure to describe their unique bounded distributions. As a result, the mean value and rate of change in each measure were different when presented on the transformed scale. The differences in the center and range of each measure were accounted for with the baseline/centering (y_{0k}) and scaling (s) parameters to relate changes in the latent variable to each measure. Both shared and unique changes were scaled with s to make parameters comparable.

Unstructured longitudinal model

Prior to structural model development, an unstructured longitudinal model was developed[28] to estimate the baseline, scaling, and Aranda-Ordaz transform coefficients for each endpoint. This was conducted using all available data, accounting for longitudinal changes with an auto-correlated individual estimate at each visit as shown in Equations 6–8. Only shared variance was accounted for during unstructured model development.

$$\Psi_{iv} = \psi_{i0} + \psi_{iv} \tag{6}$$

$$\psi_{i0} \sim N(0, 1) \tag{7}$$

$$\psi_{iv} \sim N_v(\mu, \Omega) \tag{8}$$

where Ψ is the latent variable model for individual i, at visit v, ψ_{i0} are samples from a normal distribution with mean 0 and variance 1 describing the value of Ψ at baseline, and ψ_{iv} are auto-correlated random variables sampled from a full multivariate normal distribution with estimated mean, μ, and variance-covariance matrix, Ω, with dimensions v x v for each non-baseline visit (i.e., $v > 1$).

The direction of the Aranda-Ordaz transformation was tested at this stage of model development to assess the improvement of model performance by using the more flexible lower portion of the transform.[29] This was done by mapping the lower and upper boundaries of the observed data to either their respective boundaries (matched) or their opposing boundaries (flipped) on the transformed scale and selecting the model based on model fit (Equations 9 and 10).

$$s_{\text{flipped}} = -s_{\text{matched}} \tag{9}$$

$$y_{\text{flipped}} = b - \left(y_{\text{matched}} - a\right) \tag{10}$$

where s represents the scaling parameter, a and b represent the lower and upper boundary and y represents variables related to the dependent variable including: observations, y_{ijk}; individual predictions, $\hat{y}_{ijk}$; lowest and highest observed values, y_l and y_u; and the baseline population prediction, y_{0k}.

Given the baseline, scaling, and transform coefficients were prone to multicollinearity, the estimated baseline and transform coefficients for each endpoint from the unstructured model were fixed before proceeding to structural model development to improve the stability of the model.[28] Shared variance and scaling parameters were chosen not to be fixed to allow the inclusion of covariates to reduce the unexplained variability of the model.

Structural model

Structural model development was conducted making sequential changes to an initial exposure–response model structure. This consisted of a placebo effect, independent hyperbolic E_{max} exposure–response relationships for both ervogastat and clesacostat driven by individual predicted average drug concentrations derived by the pharmacokinetic analyses, and an asymptotic exponential longitudinal model shared by placebo and drug effects. The pharmacodynamic effects of each drug were initially assumed to be additive, with pharmacodynamic interactions being tested using the general pharmacodynamic interaction (GPDI) model.[30] Random effects representing IIV were considered for shared and unique variance of baseline liver fat and the shared placebo effect. Both the IIV and residual unexplained variability (RUV) were assumed to be normally distributed within the dynamic transform.

Covariate model

The structural model was used to conduct covariate analysis with pre-specified covariates of interest (Table S5). Missing covariates were imputed using the median or mode values for continuous and categorical covariates, respectively. Subjects without any phenotype information for PNPLA3 were treated as the reference population, as substantial differences in placebo response between this group and the C/C phenotype prevented them from being grouped together. Both continuous and categorical covariates were applied to parameters on the transformed scale prior to scaling and were parameterized assuming an additive effect (Equations 11 and 12).

$$P = \theta_P + \theta_{cov} \cdot cov_i \tag{11}$$

$$P = \theta_P + \left(\log\left(cov_i\right) - \log\left(cov_{ref}\right)\right) \cdot \theta_{cov} \tag{12}$$

where P is the population parameter for individuals with covariate value, cov_i, with values of 0 and 1 for categorical covariates and values greater than 0 for continuous covariates, cov_{ref} is the median value for a continuous covariate and θ_{cov} is the estimable covariate effect parameter.

Covariate analysis was conducted using a stepwise procedure.[31] Covariate screening was conducted prior to analysis to identify independent and statistically significant covariates. Screened covariates were then assessed as part of a standard forward-selection backward-elimination procedure. Both screening and forward-selection used an alpha level of 0.01, while backward elimination used an alpha level of 0.001.

Model software and evaluation

Models were developed using non-linear mixed effects methods in NONMEM® Version VII Level 5.0 using Perl speaks NONMEM® (PsN).[32,33] Exploratory analysis, model diagnostic plots, and post-processing of NONMEM® output were generated using the R statistical and programming language.[34]

Model evaluation was conducted at each step of model development and consisted of assessing changes in the objective function value, standard goodness-of-fit diagnostics, and visual predictive checks with or without prediction–correction.[35,36] When using dTBS, normalized prediction distribution errors (NPDE) were used for the assessment of model misspecification due to the need to explicitly define the log-likelihood.[37] Autocorrelation plots were used during exposure–response model development to identify any systematic variation in endpoints that were not explained by the latent variable. Final model parameter uncertainty was evaluated using sampling importance resampling (SIR).[38]

Model simulation

Simulations assessing the impact of covariates on the pharmacodynamics of MRI-PDFF and CAP™ over time were performed for a 300/10 mg BID dose over 6 weeks. The reference population (defined as having the median and mode values for continuous and categorical covariates) was compared to the 5th and 95th percentiles for continuous covariates or each category for categorical covariates.

A clinical trial simulation of NCT04399538 with the aim of testing investigated and hypothetical dosing regimens was conducted to assess the predicted efficacy of ervogastat with lower clesacostat doses. Simulations used the existing 6-week study design of 15 participants with presumed NASH in each treatment arm administered total daily doses of 25/5 to 600/20 mg of ervogastat/clesacostat given either once or twice daily. Clinical trials simulations consisted of 1000 simulations and included variability from model uncertainty from SIR, IIV and RUV. Covariates for simulated individuals were sampled from observed combinations in NCT04399538 participants.

RESULTS

Study data

The data used for analyses consisted of 260, 487, and 524 subjects for ervogastat PK, clesacostat PK and ER modeling, respectively. Of the 3648 measured ervogastat concentrations and 6928 measured clesacostat concentrations, 3353 and 6722 were considered evaluable, respectively, with the remainder (8% and 3%) being below the lower limit of quantification. These samples were excluded from the analysis, as the low proportion of samples below the limit of quantification was deemed unlikely to introduce sufficient bias to warrant the use of methods for handling censored observations.[39] Of the 1398 MRI-PDFF measurements, none were at the lower or upper bound (0–100%), while the 1702 CAP measurements had 3 and 66 values at the lower and upper bound (100–400 dB/m), respectively (Figure 1). The method chosen for exposure–response allowed no data to be excluded during analysis.[25] All MRI-PDFF measurements had a corresponding CAP measurement, either at baseline or at the same visit. Table 1 presents a summary of the demographics represented in the analysis dataset.

Pharmacokinetic model

The final PK model developed to describe ervogastat was a two-compartment kinetic model with parallel first- and zero-order absorption with absorption-lag on the zero-order component and inter-individual variability on apparent clearance and apparent central volume of distribution. Random unexplained variability was explained with a combined additive and proportional residual error model. Clesacostat concentrations were best described by a two-compartment kinetic model with first-order absorption and inter-individual variability on apparent clearance. Random unexplained variability was explained with a combined error model, consisting of an additive and a time-varying proportional component. A full description of PK model results can be found in the Supporting Information.

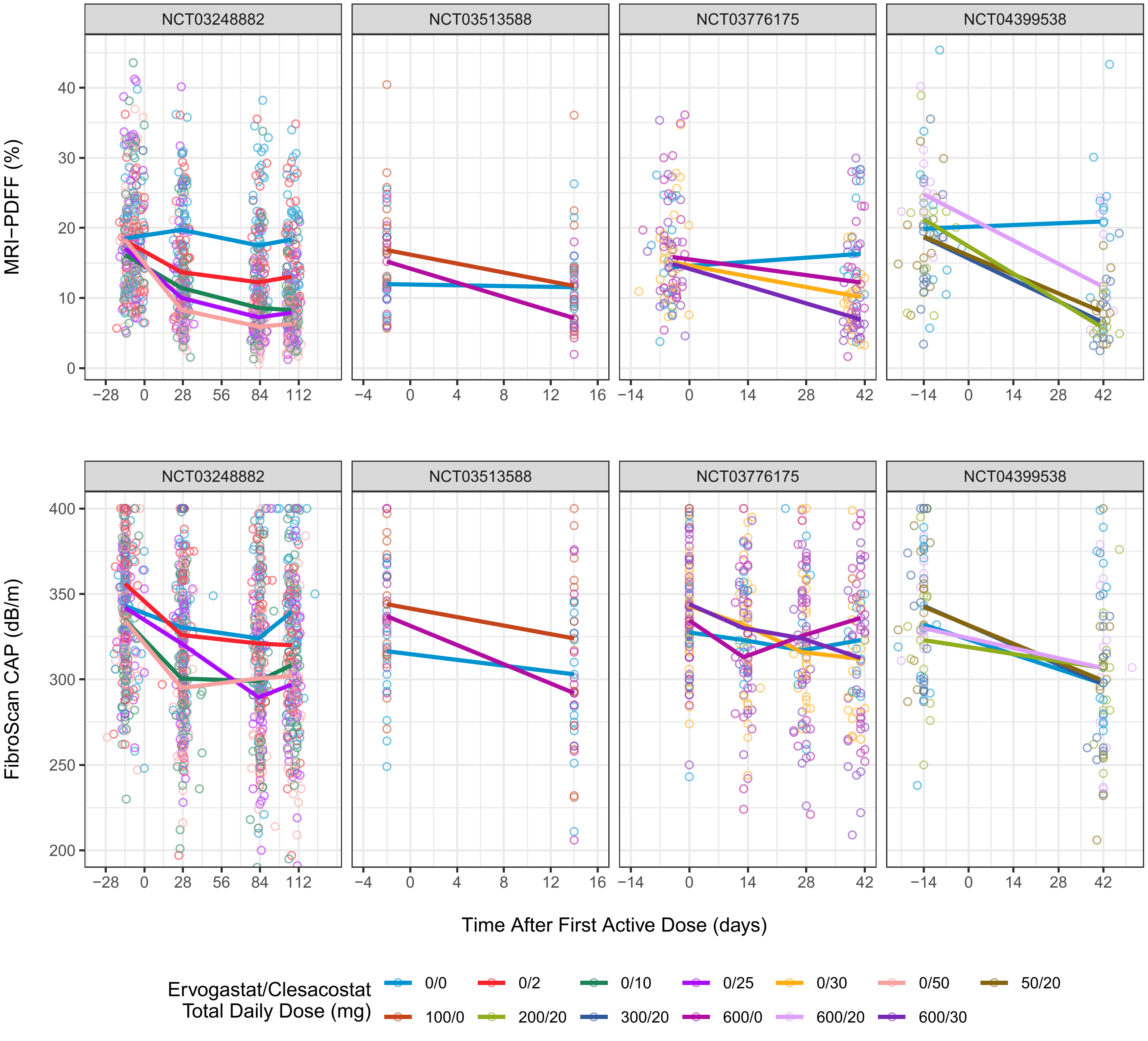

FIGURE 1 Longitudinal profile of observed data. Colored points represent the observed MRI-PDFF (top) and FibroScan® CAP™ (bottom) data for different ervogastat/clesacostat dosing regimens. Colored lines represent the median of the observed data at each study visit.

TABLE 1 Summary of demographics in analysis populations.

	Ervogastat PopPK		Clesacostat PopPK		Exposure–Response	
Variable	**Mean (SD)**	**Median (range)**	**Mean (SD)**	**Median (range)**	**Mean (SD)**	**Median (range)**
Age (years)	47.7 (12)	49 (18, 72)	49.9 (13.1)	52 (19, 72)	53 (11.4)	55 (19, 72)
Body weight (kg)	92.5 (18.2)	91 (58.4, 152)	92.6 (18.5)	90 (52, 170)	96.5 (19)	93.8 (55, 170)
Body mass index	31.6 (5.73)	31.1 (19, 49)	32.2 (5.79)	31.8 (19, 56)	34.4 (5)	33.6 (24, 56)
ALT	35.7 (26.6)	27.5 (9, 182)	43.1 (33.6)	33 (5, 302)	48.5 (34.3)	40 (6, 341)
AST	28.2 (17.7)	24 (11, 179)	33.2 (22.6)	26 (6, 179)	34.6 (21.7)	28 (10, 192)
GGT	43.4 (36.8)	32 (8, 242)	50.8 (47)	34 (9, 329)	48.6 (40.2)	35 (9, 254)
Triglycerides	150 (82)	131 (37, 625)	157 (92.6)	137 (39, 697)	177 (90.5)	159 (50, 697)
Total cholesterol	178 (42.3)	180 (66.2, 307)	185 (39.8)	183 (96, 345)	187 (39)	185 (95, 330)
HDL	45.2 (11.2)	43 (23, 82)	46.6 (12.1)	45 (20, 92)	45 (11.5)	44 (20, 92)
LDL	111 (33.4)	108 (48, 193)	114 (35.4)	112 (29, 269)	113 (34.7)	110 (29, 225)
Platelets ($\times 10^9$/L)	238 (58.9)	237 (29, 458)	244 (64.5)	244 (34, 544)	256 (61.5)	252 (104, 544)
EGFR (mL/min)	94.8 (17.3)	95 (29, 152)	94.5 (17.4)	95.3 (29, 141)	93.1 (16.6)	94.3 (29, 138)
Creatinine (mg/dL)	0.884 (0.182)	0.89 (0.48, 1.4)	0.854 (0.194)	0.81 (0.48, 1.5)	0.813 (0.176)	0.8 (0.48, 1.5)

	Ervogastat PopPK		Clesacostat PopPK		Exposure–Response	
Variable	**Count**	**Percent**	**Count**	**Percent**	**Count**	**Percent**
Sex						
Male	189	72.7	294	60.4	262	50
Female	71	27.3	193	39.6	262	50
Race						
White	187	71.9	344	70.6	434	82.8
Black	50	19.2	62	12.7	21	4
Asian	19	7.3	56	11.5	56	10.7
Other	4	1.5	25	5.1	13	2.5
Patient status						
Healthy volunteer	86	33.1	117	24	–	–
Mild Hep. Impaired	6	2.3	6	1.2	–	–
Mod. Hep. Impaired	6	2.3	6	1.2	–	–
Sev. Hep. Impaired	6	2.3	6	1.2	–	–
NAFLD	101	38.8	132	27.1	244	46.6
Presumed NASH	55	21.2	220	45.2	280	53.4
SLCO1B1 phenotype						
EM	44	16.9	298	61.2	240	45.8
IM	10	3.8	88	18.1	84	16
PM	NA	NA	16	3.3	16	3.1
Not determined	206	79.2	85	17.5	184	35.1
PNPLA3 phenotype						
C/C	16	6.2	95	19.5	119	22.7
C/G	25	9.6	107	22	142	27.1
G/G	13	5	65	13.3	79	15.1
Not determined	206	79.2	220	45.2	184	35.1

Abbreviations: ALT, alanine transaminase; AST, aspartate transaminase; EGFR, estimated glomerular filtration rate; EM, extensive metabolizer; GGT, gamma-glutamyl transferase; HDL, high-density lipoprotein; IM, intermediate metabolizer; Hep. Impaired, hepatic impaired; LDL, low-density lipoprotein; Mod., moderate; NAFLD, non-alcoholic fatty liver disease; NASH, non-alcoholic steatohepatitis; PM, poor metabolizer; PNPLA3, patatin-like phospholipase domain-containing 3; SD, standard deviation; Sev., severe; SLCO1B1, solute carrier organic anion transporter family member 1B1.

Exposure–response model

Unstructured longitudinal model

Four permutations of the unstructured longitudinal model were tested to assess the direction of the Aranda-Ordaz transform for each endpoint alone and together. The combination of using matched boundaries on MRI-PDFF and flipped boundaries on CAP™ provided the best overall fit, while also being resilient to changes in initial parameter estimates. This result matched expectations based on the distribution of CAP™ observations being most dense at the upper boundary (Figure 2).

Structural model

Parameters for the full common factor model were successfully estimated, with an improved fit and similar predictions to the unstructured longitudinal model. The unique variance on MRI-PDFF had a small magnitude and high correlation with the latent variable and was removed. The unique variance of CAP™ measures was removed to assess whether it was necessary. When doing so, NPDE became highly auto-correlated to the next three observations, implying that the unique variance was accounting for a systematic trend in CAP™ data that was independent of the latent variable (Figure S7).

The model was further developed into a parsimonious structural model consisting of an asymptotic exponential longitudinal model with a separate rate constant for placebo and a shared rate constant for ervogastat and clesacostat effect. In addition to the random effects described in Equations 2–4, IIV was also estimated on the maximum placebo effect. Drug effect was initially described by a hyperbolic Emax model for both clesacostat and ervogastat. The EC_{50} for ervogastat was not identifiable and was reduced to a treatment-effect model due to limited dose-ranging monotherapy data. The combined effect of ervogastat and clesacostat was found to be less than additive, where the GPDI model was reduced to a treatment effect where co-administration of clesacostat reduced the effect of ervogastat. Key model development steps are outlined in Table S6.

Covariate model

During direct screening of covariates, the impact of covariates on key model parameters was assessed when applied to both endpoints simultaneously or separately by influencing the shared latent variable or endpoint-specific

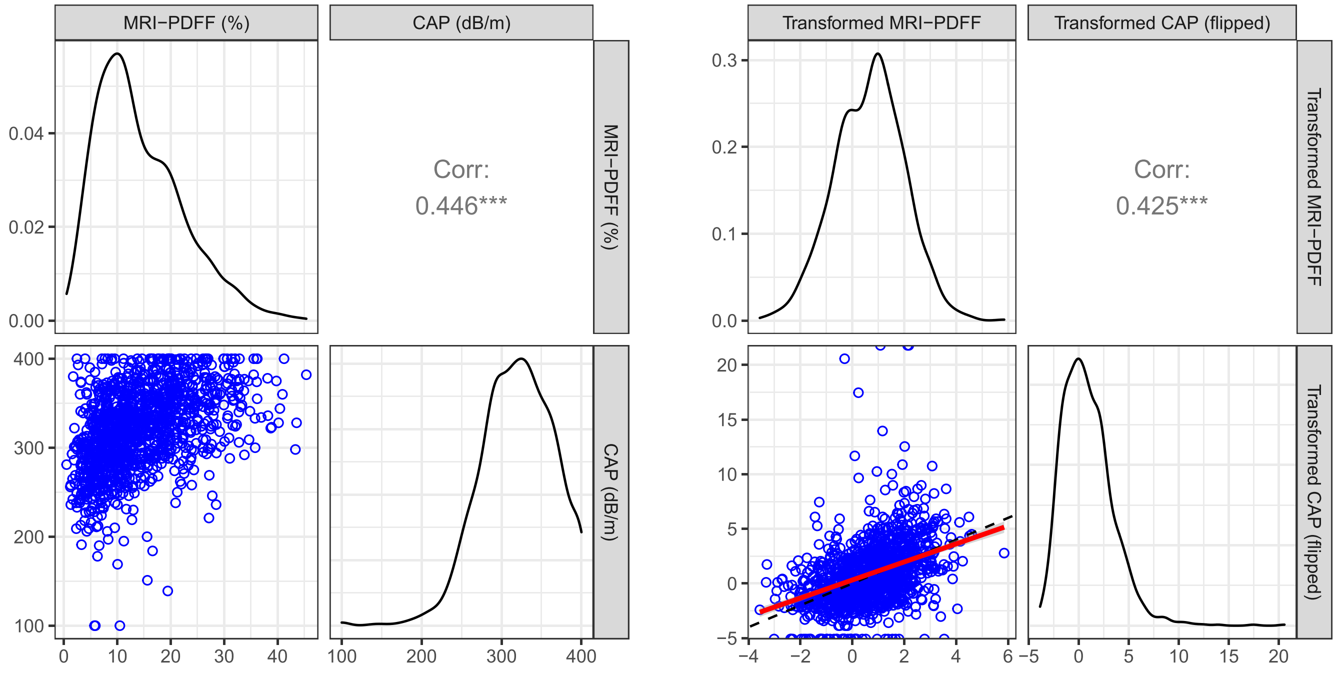

FIGURE 2 Distribution of untransformed and transformed observed data. Plots show different representations of the distribution of MRI-PDFF and FibroScan® CAP™ data when untransformed (left grid) and transformed (right grid). Upper left and lower left density plots show an estimate of the probability density function for each variable. The lower left and upper right sections show the correlation between these variables using a scatter plot and the calculated Pearson's correlation coefficient with asterisks denoting the significance of the correlation (****p*-value <0.001). The red line represents a linear regression of the transformed MRI-PDFF and CAP™ variables. Both the linear regression and Pearson's correlation coefficient for transformed data are estimated on non-boundary data only.

TABLE 2 Final exposure–response model parameter estimates.

Label	Value	95% CI[b]	Shk.
Objective function value	24,358	–	–
Condition number[a]	6.14	–	–
Population parameter	–	–	–
Baseline liver fat via MRI on transformed scale; $h(z(\mathrm{BSL}_{\mathrm{MRI}}))$	−1.16	Fixed	–
Baseline liver fat via CAP™ on transformed scale; $h(z(\mathrm{BSL}_{\mathrm{CAP}}))$	5.05	Fixed	–
Half-life of placebo effect rate constant; $t_{½,\mathrm{kpbo}}$ (days)	49.1	39.1, 63.7	–
Shared half-life of drug effect rate constant; $t_{½,\mathrm{ktrt}}$ (days)	18.8	17.4, 20.2	–
Maximum placebo effect on transformed scale; $P_{\max}$	0.393	0.124, 0.659	–
Ervogastat treatment effect on transformed scale; $E_{\mathrm{trt,er}}$	1.27	0.940, 1.57	–
Clesacostat maximum effect on transformed scale; $E_{\mathrm{emax,cl}}$	2.32	2.05, 2.58	–
Concentration where 50% of $E_{\mathrm{emax,cl}}$ occurs; $EC_{50,\mathrm{cl}}$ (ng/mL)	389	306, 599	–
Inhibition of $E_{\mathrm{trt,er}}$ by clesacostat treatment; $I_{\mathrm{trt,cl\text{-}er}}$	−0.735	−0.897, −0.557	–
MRI Aranda-Ordaz transformation parameter; α_{MRI}	4.92	Fixed	–
CAP™ Aranda-Ordaz transformation parameter; α_{CAP}	32.1	Fixed	–
MRI residual standard deviation on transformed scale; σ_{MRI}	0.205	0.192, 0.219	–
CAP™ residual standard deviation on transformed scale; σ_{CAP}	5.35	5.12, 5.59	–
MRI scaling of transformed variable; s_{MRI}	0.698	0.656, 0.743	–
Negative CAP™ scaling of transformed variable; $-s_{\mathrm{CAP}}$	2.77	2.50, 3.07	–
Shared effect of baseline ALT on $h(z(\mathrm{BSL}_{\psi}))$; ref. 40 IU	0.575	0.430, 0.716	–
Effect of baseline weight on $h(z(\mathrm{BSL}_{\mathrm{CAP}}))$; ref. 92 kg	3.80	2.99, 4.67	–
Effect of inpatient study design on $P_{\max}$	−2.74	−3.68, −1.78	–
Effect of PNPLA3 C/C phenotype on $P_{\max}$	−1.00	−1.31, −0.693	–
Effect of PNPLA3 C/G phenotype on $P_{\max}$	−0.694	−1.01, −0.387	–
Effect of PNPLA3 G/G phenotype on $P_{\max}$	−0.0835	−0.442, 0.278	–
Shared effect of age on $h(z(\mathrm{BSL}_{\psi}))$; ref. 51 years	−0.564	−0.899, −0.234	–
Inter-study variability			
Shared baseline liver fat; $\omega_{\mathrm{BSL}\psi}$ (SD)	1.00	Fixed	4.13
Unique baseline CAP™; $\omega_{\mathrm{BSL,CAP}}$ (SD)	1.33	1.16, 1.53	24.1
Maximum placebo effect; ω_{Pmax} (SD)	0.959	0.840, 1.08	24.6
Random unexplained variability			
MRI additive error in transformed scale; $\varepsilon_{\mathrm{MRI}}$ (SD)	1.00	Fixed	32.5[c]
CAP™ additive error in transformed scale; $\varepsilon_{\mathrm{CAP}}$ (SD)	1.00	Fixed	13.7[c]

Abbreviations: ALT, alanine transaminase; CAP™, FibroScan® controlled attenuation parameter; CI, asymptotic confidence intervals; MRI, magnetic resonance imaging estimated proton density fat fraction; PNPLA3, patatin-like phospholipase domain-containing protein 3; ref., reference value used for covariate parameterization; SD, standard deviation; Shk., shrinkage of η and ε.

[a] Condition number defined as the square root of the ratio of largest to smallest eigenvalues of the correlation matrix.

[b] 95% confidence intervals calculated using sampling importance resampling.

[c] Values at boundaries were excluded when calculating epsilon shrinkage.

parameters, respectively (Table S7). While most significant covariates applied to both baseline MRI-PDFF and CAP™ (shared baseline), body weight was found to have a higher impact on CAP™ baseline than the MRI-PDFF baseline. This was also identified during stepwise covariate modeling, where only the effect of body weight on CAP™ was retained in the final model. The final set of covariates also included the effect of ALT and age on shared baseline, and the effect of inpatient status and PNPLA3 phenotype on placebo effect. Subjects without any phenotype information for PNPLA3 were treated as the reference population, as substantial differences in placebo response between this group and the C/C phenotype prevented them from being grouped together.

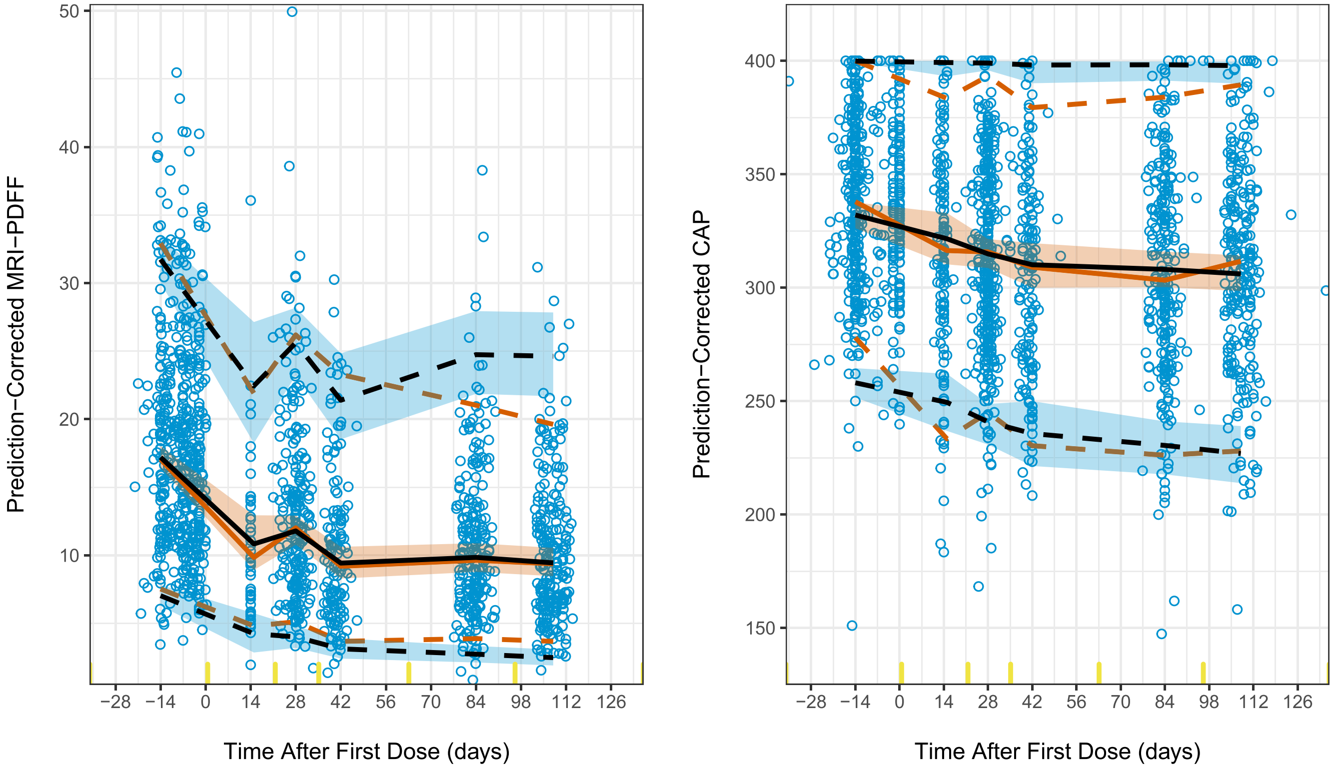

FIGURE 3 Prediction-Corrected Visual Predictive Check for MRI-PDFF and CAP™ Endpoints. The binned prediction-corrected observed data are represented by blue circles and orange-red lines (solid line—median; dashed lines – 5th and 95th percentiles). The binned prediction-corrected simulated MRI-PDFF and CAP™ based on 1000 simulations of the index population is represented by the black solid line and orange-red ribbon (median and 95% prediction interval (PI) of the median, respectively) and by the black dashed lines and blue ribbons (median and 95% PI of the 5th and 95th percentiles, respectively). The yellow notches at the bottom of the plot represent the cutpoints used for binning. CAP™, FibroScan® controlled attenuation parameter; MRI-PDFF, magnetic resonance imaging estimated proton density fat fraction; PI, prediction intervals.

Table 2 shows the parameter estimates for the final model. CAP™ values at the lower boundary (100 dB/m) were identified as outliers with absolute NPDEs >30 and were removed prior to the estimation of the final model parameters. No significant changes in parameter values were observed in the removal of outliers. The prediction-corrected VPC (Figure 3) for both endpoints shows the model describes the data adequately, with some misspecification highlighted by the 95% prediction intervals at later times or near the upper bound for MRI-PDFF and CAP™, respectively, where higher variability was predicted than observed.

Model simulation

Simulations assessing the effect of age, ALT, body weight, and PNPLA3 phenotype on liver fat measures are shown in Figure 4. The mean and 90% CI of the percent change from baseline of each PD endpoint observed in the 1000 simulated clinical trials using the NCT04399538 study design can be found in Table 3. Dose-ranging simulations could only be performed for clesacostat, but show the extent of efficacy lost upon reducing clesacostat doses.

DISCUSSION

Through the use of PK/PD modeling, the PK and exposure–response relationships of ervogastat and clesacostat were described. The effect of the two therapies in combination was found to be less than additive but provided greater efficacy than when given alone, showing their pharmacotherapeutic profile was improved with combination therapy. While it could not be used to assess differences in ervogastat dosing, clinical trial simulation highlighted that clesacostat doses of interest were not at the maximum, providing context when considering the maximum tolerated dose of clesacostat.

Covariate analysis highlighted the impact of alanine transaminase (ALT) and age on baseline liver fat which are consistent with the pathophysiology of NASH, where elevated ALT reflects the extent of liver injury and, therefore, liver fat in patients, and increased age being associated with

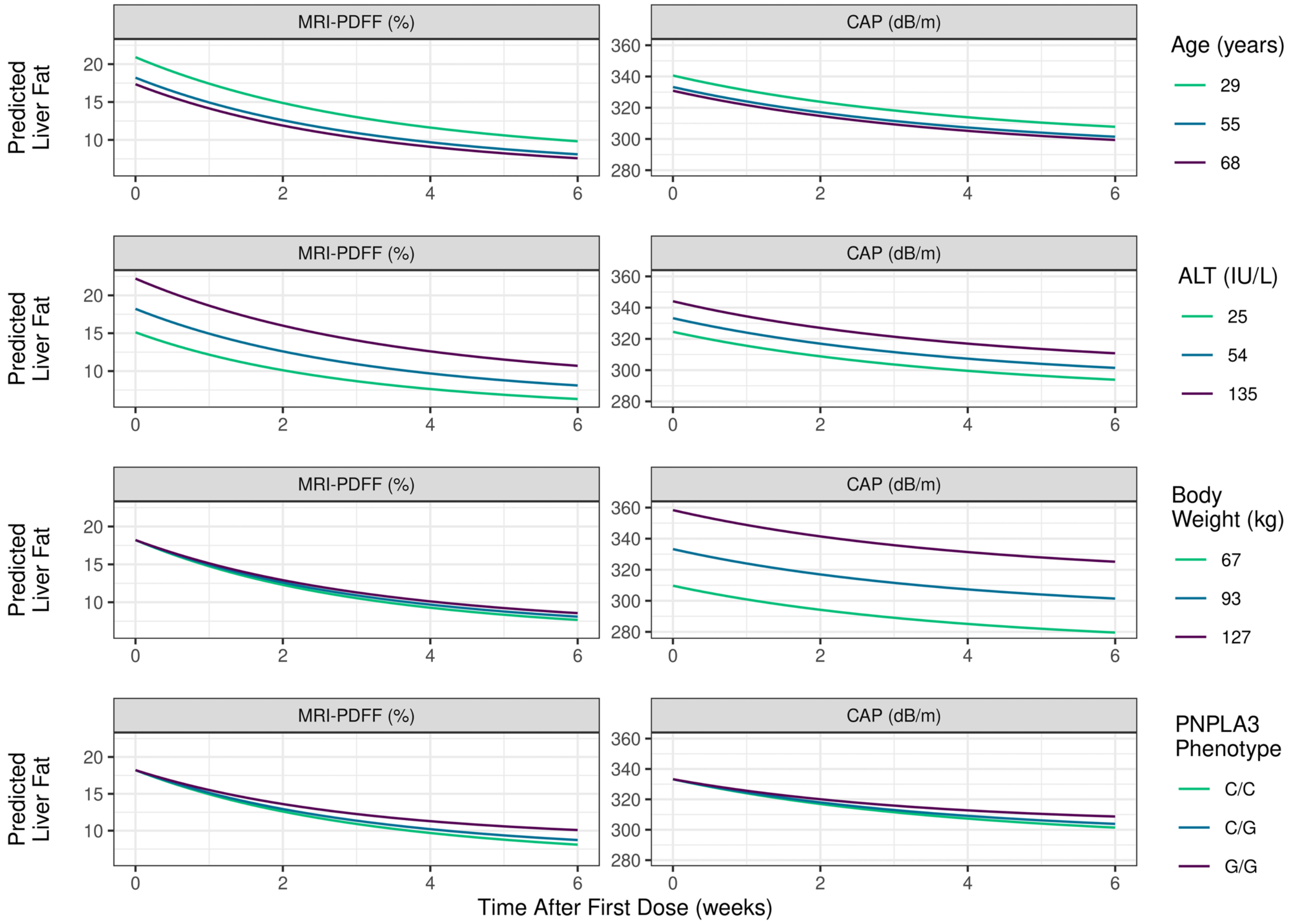

FIGURE 4 Covariate Effects on Population Typical Liver Fat Over 6 weeks. Solid lines represent the population prediction of MRI-PDFF (left) and CAP™ (right) over 6 weeks of 300/10 mg twice daily ervogastat/clesacostat. Reference predictions (median and mode values for continuous and categorical covariates in presumed NASH populations) are compared to the 5th and 95th percentile or each category of covariates included in the model.

disease progression to more severe forms of NASH where lower liver fat but higher fibrosis is observed.[40–43] The larger liver fat reduction seen in the ervogastat Phase 1b study in NAFLD patients (NCT03513588) was attributed to a larger placebo effect, explained by the inpatient study design and lower severity of disease in this population. Subjects with the G/G PNPLA3 phenotype were found to have a lower liver fat reduction consistent with the more severe liver disease and disease progression seen in these patients.[44]

The systematic variation observed in CAP™ required the addition of a separate random effect. This is supported by findings that CAP™ may be influenced by factors other than the underlying liver fat.[45] Given the FibroScan® sensitivity to an individual's skin-liver capsule distance,[46] this systematic variance may come from interference from excess body fat as indicated by the higher impact of baseline body weight on baseline CAP™ in comparison to baseline MRI-PDFF. This suggests that therapies that cause weight loss in addition to liver fat reduction may show a different correlation between MRI-PDFF and CAP™ than medications not associated with weight loss.

The size of FibroScan® probe (M vs. XL) could also be considered as a covariate to describe the unexplained variability in the CAP™ endpoint. As XL probe usage instructions for the FibroScan® equipment is based on body weight, this covariate was deemed unlikely to be the cause of any differences in assessments and has been shown to have negligible impact on assessments when comparing results from both M and XL probes within the same individual.[47]

Despite the physiological basis behind this interpretation of the unique variance for CAP™, it is severely limited by the low number of endpoints used to characterize the latent variable. Without 3–4 endpoints to inform the latent variable, it is possible that only the variance in one of the two endpoints is captured rather than the shared variance between them. If this were the case, the unique variance of CAP may represent the systematic difference between the two methods rather than bias in determining

TABLE 3 Observed and simulated liver fat reduction for in vitro and in silico NCT study.

	MRI-PDFF (%)		FibroScan CAP™ (dB/m)	
Ervogastat/Clesacostat treatment regimen	**Observed**[a]	**Predicted**	**Observed**[a]	**Predicted**
25/10 mg BID	−52.4	−45.7 (−60.5, −31.1)	−6.45	−7.35 (−15.8, 1.45)
100/10 mg BID	−56.6	−45.4 (−60.8, −30.8)	−1.69	−7.24 (−15.9, 1.39)
300/20 mg QD	−58.8	−45.9 (−60.9, −31.1)	−5.60	−7.40 (−16.5, 1.06)
300/10 mg BID	−45.8	−45.6 (−61.6, −31.8)	−3.57	−7.48 (−16.3, 1.28)
300/5 mg BID	–	−37.4 (−53.0, −21.6)	–	−5.57 (−14.2, 2.75)
300/2.5 mg BID	–	−28.9 (−45.0, −13.5)	–	−4.29 (−12.8, 4.78)

Note: Values represent placebo-corrected percent change from baseline.

Abbreviations: BID, twice daily; CAP™, FibroScan® controlled attenuation parameter; MRI-PDFF, magnetic resonance imaging estimated proton density fat fraction; QD, once daily.

[a] Adjusted geometric least-squares mean.

the underlying steatosis. Further work is needed to describe a latent variable that is a better representation of steatosis and could be achieved through the addition of other direct measurements, such as ultrasound-derived fat fraction[48] or the NAFLD activity sub-score for steatosis derived from biopsy.[8]

Given the similarities in assumptions between the present analysis and IRT, this approach could be considered an item characteristic function for continuous data and may be appropriate for other methods that map continuous data to a latent space. For example, it may be feasible to leverage continuous data with a single boundary using a dTBS approach with the Box-Cox transform.[24] Other methods for handling continuous-bounded outcomes data such as beta regression and the bounded integer model also appear to be compatible with IRT.[49,50]

These other methods would also be compatible with the present analysis, being able to account for the bias associated with mishandling continuous-bounded data and bringing the same limitation of parameter estimates not being directly interpretable. These were not chosen in favor of the parsimony in defining possible outcomes that come with the dTBS method.

A limitation of the present work comes from the use of average concentrations to drive exposure response, rather than using a longitudinal indirect response model. While the chosen method was able to account for the pharmacodynamic delay between dosing and liver fat reduction, the parameter estimate describing this delay is a combination of both pharmacokinetic and pharmacodynamic delay reducing the interpretability of parameter values.

The present study used population modeling to describe the pharmacokinetics of ervogastat and clesacostat and their subsequent exposure–response relationships on liver fat. Using a dynamic transformation, both MRI-PDFF and FibroScan® CAP™ were able to be modeled simultaneously with a single latent variable representing liver fat. This provided a longitudinal description of MRI-PDFF for ervogastat finding that current doses achieve maximum effect, despite having limited data. This approach provides a good basis for further model development, potentially allowing for all liver fat information (including biopsy results) to be incorporated for support of Phase 3 dose selection.

AUTHOR CONTRIBUTIONS

All authors wrote the manuscript. J.H.H., N.B.A., and M.V. designed the research. J.H.H. and J.W. performed the research. J.H.H. analyzed the data.

FUNDING INFORMATION

These studies were sponsored by Pfizer.

CONFLICT OF INTEREST STATEMENT

All authors were full-time employees of Pfizer during the study conduct.

DATA AVAILABILITY STATEMENT

Upon request, and subject to review, Pfizer will provide the data that support the findings of this study. Subject to certain criteria, conditions, and exceptions, Pfizer may also provide access to the related individual de-identified participant data. See https://www.pfizer.com/science/clinical-trials/trial-data-and-results for more information.

ORCID

Jim H. Hughes https://orcid.org/0000-0002-1862-5805
Neeta B. Amin https://orcid.org/0000-0002-0727-4683
Jessica Wojciechowski https://orcid.org/0000-0002-3302-8742

REFERENCES

1. Haas JT, Francque S, Staels B. Pathophysiology and mechanisms of nonalcoholic fatty liver disease. *Annu Rev Physiol.* 2016;78(1):181-205. doi:10.1146/annurev-physiol-021115-105331

2. Fon Tacer K, Rozman D. Nonalcoholic fatty liver disease: focus on lipoprotein and lipid deregulation. *J Lipids*. 2011;2011:783976. doi:10.1155/2011/783976
3. Younossi ZM, Koenig AB, Abdelatif D, Fazel Y, Henry L, Wymer M. Global epidemiology of nonalcoholic fatty liver disease—meta-analytic assessment of prevalence, incidence, and outcomes. *Hepatology*. 2016;64(1):73-84. doi:10.1002/hep.31173
4. Zobair MY, Maria S, Youssef Y, et al. Epidemiology of chronic liver diseases in the USA in the past three decades. *Gut*. 2020;69(3):564-568. doi:10.1136/gutjnl-2019-318813
5. Witkowski M, Moreno SI, Fernandes J, Johansen P, Augusto M, Nair S. The economic burden of non-alcoholic steatohepatitis: a systematic review. *PharmacoEconomics*. 2022;40(8):751-776. doi:10.1007/s40273-022-01140-y
6. Parthasarathy G, Revelo X, Malhi H. Pathogenesis of non-alcoholic steatohepatitis: An overview. *Hepatol Commun*. 2020;4(4):478-492. doi:10.1002/hep4.1479
7. Brunt EM, Kleiner DE, Carpenter DH, et al. NAFLD: reporting histologic findings in clinical practice. *Hepatology*. 2021;73(5):2028-2038. doi:10.1002/hep.31599
8. Kleiner DE, Brunt EM, Van Natta M, et al. Design and validation of a histological scoring system for nonalcoholic fatty liver disease. *Hepatology*. 2005;41(6):1313-1321. doi:10.1002/hep.20701
9. Bedossa P, Poitou C, Veyrie N, et al. Histopathological algorithm and scoring system for evaluation of liver lesions in morbidly obese patients. *Hepatology*. 2012;56(5):1751-1759. doi:10.1007/s10620-017-4638-3
10. Pournik O, Alavian SM, Ghalichi L, et al. Inter-observer and intra-observer agreement in pathological evaluation of non-alcoholic fatty liver disease suspected liver biopsies. *Hepat Mon*. 2014;14(1):e15167. doi:10.5812/hepatmon.15167
11. Sasso M, Beaugrand M, de Ledinghen V, et al. Controlled attenuation parameter (CAP): a novel VCTE™ guided ultrasonic attenuation measurement for the evaluation of hepatic steatosis: preliminary study and validation in a cohort of patients with chronic liver disease from various causes. *Ultrasound Med Biol*. 2010;36(11):1825-1835. doi:10.1016/j.ultrasmedbio.2010.07.005
12. Caussy C, Reeder SB, Sirlin CB, Loomba R. Noninvasive, quantitative assessment of liver fat by MRI-PDFF as an endpoint in NASH trials. *Hepatology*. 2018;68(2):763-772. doi:10.1002/hep.29639
13. Jung J, Han A, Madamba E, et al. Direct comparison of quantitative US versus controlled attenuation parameter for liver fat assessment using MRI proton density fat fraction as the reference standard in patients suspected of having NAFLD. *Radiology*. 2022;304(1):75-82. doi:10.1056/NEJMoa1701329
14. Tacke F, Horn P, Wai-Sun Wong V, et al. EASL–EASD–EASO clinical practice guidelines on the management of metabolic dysfunction-associated steatotic liver disease (MASLD). *J Hepatol*. 2024;81(3):492-542. doi:10.1016/j.jhep.2024.04.031
15. Tilg H, Byrne CD, Targher G. NASH drug treatment development: challenges and lessons. *Lancet Gastroenterol Hepatol*. 2023;8(10):943-954. doi:10.1016/S2468-1253(23)00159-0
16. Calle RA, Amin NB, Carvajal-Gonzalez S, et al. ACC inhibitor alone or co-administered with a DGAT2 inhibitor in patients with non-alcoholic fatty liver disease: two parallel, placebo-controlled, randomized phase 2a trials. *Nat Med*. 2021;27(10):1836-1848. doi:10.1016/S0168-8278(20)31392-1
17. An Z, Liu Q, Zeng W, et al. Relationship between controlled attenuated parameter and magnetic resonance imaging-proton density fat fraction for evaluating hepatic steatosis in patients with NAFLD. *Hepatol Commun*. 2022;6(8):1975-1986. doi:10.1002/hep4.1948
18. Caussy C, Alquiraish MH, Nguyen P, et al. Optimal threshold of controlled attenuation parameter with MRI-PDFF as the gold standard for the detection of hepatic steatosis. *Hepatology*. 2018;67(4):1348-1359. doi:10.1002/hep.29797
19. Amin NB, Darekar A, Anstee QM, et al. Efficacy and safety of an orally administered DGAT2 inhibitor alone or coadministered with a liver-targeted ACC inhibitor in adults with non-alcoholic steatohepatitis (NASH): rationale and design of the phase II, dose-ranging, dose-finding, randomised, placebo-controlled MIRNA (metabolic interventions to resolve NASH with fibrosis) study. *BMJ Open*. 2022;12(3):e056159. doi:10.1136/bmjopen-2021-056159
20. Bergman A, Carvajal-Gonzalez S, Tarabar S, Saxena AR, Esler WP, Amin NB. Safety, tolerability, pharmacokinetics, and pharmacodynamics of a liver-targeting acetyl-CoA carboxylase inhibitor (PF-05221304): a three-part randomized phase 1 study. *Clin Pharmacol Drug Dev*. 2020;9(4):514-526. doi:10.1002/cpdd.782
21. Amin NB, Saxena AR, Somayaji V, Dullea R. Inhibition of diacylglycerol acyltransferase 2 versus diacylglycerol acyltransferase 1: potential therapeutic implications of pharmacology. *Clin Ther*. 2023;45(1):55-70. doi:10.1016/j.clinthera.2022.12.008
22. Gastonguay MR. Full covariate models as an alternative to methods relying on statistical significance for inferences about covariate effects: a review of methodology and 42 case studies. Paper Presented at: Population Approach Group Europe; 2011 Jun 7–10; Athens, Greece. Accessed August 2, 2022. https://www.page-meeting.org/?abstract=2229
23. Harrell FE Jr. Multivariable modeling strategies. In: Harrell FE Jr, ed. *Regression Modeling Strategies: with Applications to Linear Models, Logistic and Ordinal Regression, and Survival Analysis*. Springer International Publishing; 2015:63-102.
24. Dosne A-G, Bergstrand M, Karlsson MO. A strategy for residual error modeling incorporating scedasticity of variance and distribution shape. *J Pharmacokinet Pharmacodyn*. 2016;43(2):137-151. doi:10.1007/s10928-015-9460-y
25. Hutmacher MM, French JL, Krishnaswami S, Menon S. Estimating transformations for repeated measures modeling of continuous bounded outcome data. *Stat Med*. 2011;30(9):935-949. doi:10.1002/sim.4155
26. Woods CM, Edwards MC. Factor analysis and related methods. In: Rao CR, Miller JP, Rao DC, eds. *Handbook of Statistics 27: Epidemiology and Medical Statistics*. North-Holland Pub. Co.; 2007:367-394.
27. Hayashi K, Bentler PM, Yuan K-H. Structural equation modeling. In: Rao CR, Miller JP, Rao DC, eds. *Handbook of Statistics 27: Epidemiology and Medical Statistics*. North-Holland Pub. Co.; 2007:395-428.
28. Ueckert S. Modeling composite assessment data using item response theory. *CPT Pharmacometrics Syst Pharmacol*. 2018;7(4):205-218. doi:10.1002/psp4.12280
29. Huh Y, Wojciechowski J, Purohit VS. Moving beyond boundaries: utilization of longitudinal exposure-response model for bounded outcome score to inform decision making in the

accelerated drug development paradigm. *Clin Pharmacokinet*. 2024;63(3):381-394. doi:10.1007/s40262-024-01347-6

30. Wicha SG, Chen C, Clewe O, Simonsson USH. A general pharmacodynamic interaction model identifies perpetrators and victims in drug interactions. *Nat Commun*. 2017;8(1):2129. doi:10.1038/s41467-017-01929-y
31. Svensson RJ, Jonsson EN. Efficient and relevant stepwise covariate model building for pharmacometrics. *CPT Pharmacometrics Syst Pharmacol*. 2022;11(9):1210-1222. doi:10.1002/psp4.12838
32. Beal SL, Sheiner LB, Boeckmann A, Bauer RJ. *NONMEM User's Guides (1989–2017)*. Icon Development Solutions; 2017.
33. Lindbom L, Pihlgren P, Jonsson EN. PsN-toolkit—a collection of computer intensive statistical methods for non-linear mixed effect modeling using NONMEM. *Comput Methods Prog Biomed*. 2005;79(3):241-257. doi:10.1016/j.cmpb.2005.04.005
34. R Core Team. *R: A Language and Environment for Statistical Computing*. 4.1.1 ed. R Foundation for Statistical Computing; 2021.
35. Mould DR, Upton RN. Basic concepts in population modeling, simulation, and model-based drug development. *CPT Pharmacometrics Syst Pharmacol*. 2012;1(9):e6. doi:10.1038/psp.2013.14
36. Bergstrand M, Hooker AC, Wallin JE, Karlsson MO. Prediction-corrected visual predictive checks for diagnosing nonlinear mixed-effects models. *AAPS J*. 2011;13(2):143-151. doi:10.1208/s12248-011-9255-z
37. Comets E, Brendel K, Mentré F. Computing normalised prediction distribution errors to evaluate nonlinear mixed-effect models: the npde add-on package for R. *Comput Methods Prog Biomed*. 2008;90(2):154-166. doi:10.1016/j.cmpb.2007.12.002
38. Dosne A-G, Bergstrand M, Karlsson MO. An automated sampling importance resampling procedure for estimating parameter uncertainty. *J Pharmacokinet Pharmacodyn*. 2017;44(6):509-520. doi:10.1007/s10928-017-9542-0
39. Irby DJ, Ibrahim ME, Dauki AM, et al. Approaches to handling missing or "problematic" pharmacology data: pharmacokinetics. *CPT Pharmacometrics Syst Pharmacol*. 2021;10(4):291-308. doi:10.1002/psp4.12611
40. Noureddin M, Yates KP, Vaughn IA, et al. Clinical and histological determinants of nonalcoholic steatohepatitis and advanced fibrosis in elderly patients. *Hepatology*. 2013;58(5):1644-1654. doi:10.1002/hep.26465
41. Pirimoğlu B, Sade R, Polat G, İşlek A, Kantarcı M. Analysis of correlation between liver fat fraction and AST and ALT levels in overweight and obese children by using new magnetic resonance imaging technique. *Turk J Gastroenterol*. 2020;31(2):156-162. doi:10.5152/tjg.2020.18594
42. Wáng YXJ. Gender-specific liver aging and magnetic resonance imaging. *Quant Imaging Med Surg*. 2021;11(7):2893-2904. doi:10.21037/qims-21-227
43. Idilman R, Karatayli SC, Kabacam G, Savas B, Elhan AH, Bozdayi AM. The role of PNPLA3 (rs738409) c>g variant on histological progression of non-alcoholic fatty liver disease. *Hepatol Forum*. 2020;1(3):82-87. doi:10.14744/hf.2020.2020.0023
44. Shalimar KR, Rout G, Kumar R, Yadav R, Das P, et al. Body mass index-based controlled attenuation parameter cut-offs for assessment of hepatic steatosis in non-alcoholic fatty liver disease. *Indian J Gastroenterol*. 2020;39(1):32-41. doi:10.1007/s12664-019-00991-2
45. Karlas T, Petroff D, Sasso M, et al. Individual patient data meta-analysis of controlled attenuation parameter (CAP) technology for assessing steatosis. *J Hepatol*. 2017;66(5):1022-1030. doi:10.1016/j.jhep.2016.12.022
46. Berger A, Shili S, Zuberbuhler F, et al. Liver stiffness measurement with FibroScan: use the right probe in the right conditions! *Clin Transl Gastroenterol*. 2019;10(4):e00023. doi:10.14309/ctg.0000000000000023
47. de Lédinghen V, Hiriart J-B, Vergniol J, Merrouche W, Bedossa P, Paradis V. Controlled attenuation parameter (CAP) with the XL probe of the Fibroscan®: a comparative study with the M probe and liver biopsy. *Dig Dis Sci*. 2017;62(9):2569-2577. doi:10.1007/s10620-017-4638-3
48. Dillman JR, Thapaliya S, Tkach JA, Trout AT. Quantification of hepatic steatosis by ultrasound: prospective comparison with MRI proton density fat fraction as reference standard. *AJR Am J Roentgenol*. 2022;219(5):784-791. doi:10.2214/AJR.22.27878
49. Wellhagen GJ, Kjellsson MC, Karlsson MO. A bounded integer model for rating and composite scale data. *AAPS J*. 2019;21(4):74. doi:10.1208/s12248-019-0343-9
50. Ospina R, Ferrari SLP. A general class of zero-or-one inflated beta regression models. *Comput Stat Data Anal*. 2012;56(6):1609-1623. doi:10.1016/j.csda.2011.10.005

SUPPORTING INFORMATION

Additional supporting information can be found online in the Supporting Information section at the end of this article.

How to cite this article: Hughes JH, Amin NB, Wojciechowski J, Vourvahis M. Exposure–response modeling of liver fat imaging endpoints in non-alcoholic fatty liver disease populations administered ervogastat alone and co-administered with clesacostat. *CPT Pharmacometrics Syst Pharmacol*. 2025;14:317-330. doi:10.1002/psp4.13275